

Cite this article as: Zhao Yongqing, Wu Cong, Wang Huan. Advance in Relationship Between Tensile Strength and Toughness for 1200 MPa High Strength and High Toughness Ti-Alloy with Damage Tolerance[J]. Rare Metal Materials and Engineering, 2022, 51(12): 4389-4397.

REVIEW

Advance in Relationship Between Tensile Strength and Toughness for 1200 MPa High Strength and High Toughness Ti-Alloy with Damage Tolerance

Zhao Yongqing¹, Wu Cong², Wang Huan¹

¹Northwest Institute for Nonferrous Metal Research, Xi'an 710016, China; ²Shaanxi University of Science and Technology, Xi'an 710021, China

Abstract: High strength and high toughness Ti-alloy with damage tolerance is an important research direction of high strength titanium alloy. This work researched and reviewed the relationship among tensile strength, fracture toughness and impact toughness of 1200 MPa high strength and high toughness Ti-5321 alloy with damage tolerance. Microstructure greatly affects the tensile strength, fracture toughness and impact toughness. Lamella microstructure has good matching among tensile strength, plasticity, fracture toughness and impact toughness. Bimodal microstructure also has good matching among tensile strength, plasticity and fracture toughness, while its impact toughness is low. Based on the microstructure evolution, the changing laws of tensile strength, fracture toughness and impact toughness were analyzed. The future research direction for high strength and high toughness Ti-alloy with damage tolerance was proposed.

Key words: titanium alloy; high strength Ti-alloy with damage tolerance; mechanical property; microstructure

High strength titanium alloys (such as Ti5553, Ti-55531, BT22, Ti-1300, TB8) are an important research direction in the field of titanium alloys. Due to their good matching of strength and plasticity, high strength titanium alloys have been used in the aerospace field^[1-8]. The high strength and high toughness titanium alloy with damage tolerance is an important research content of high strength titanium alloy, which is also one of the research hotspots in the field of titanium alloys at present. Moreover, it has been applied in the aviation field due to its good matching of strength, toughness, plasticity and crack propagation rate. For example, the 1100 MPa damage tolerance titanium alloy TC21 developed by China has been applied to the in-service aircraft^[7,8], and the 1050 MPa damage tolerance titanium alloy Ti-62222S developed by the United States has been applied to the fourth generation F22 fighter aircraft^[7,8].

Compared with the properties of TC21 alloy, the strength of a new Ti alloy is expected to increase by 100 MPa, while the toughness, plasticity and crack propagation rate are not

reduced. Northwest Institute for Nonferrous Metal Research, together with Beihang University and Nanjing Technology University developed Ti-5321 (Ti-5Al-3Mo-3V-2Zr-2Cr-1Nb-1Fe) alloy^[9], whose fracture toughness can reach more than 70 MPa·m^{1/2} at the strength level of 1200 MPa. At the same time, the crack propagation rate reaches 10⁻⁵ mm/a. Through the composition design, laboratory research and further pilot study of 500 kg ingot, the properties of the prepared Ti-5321 alloy bar are: tensile strength ≥1200 MPa, elongation ≥8%, and fracture toughness ≥80 MPa·m^{1/2}.

In the recent five years, numerous studies have been carried out on the 1200 MPa high strength and high toughness Ti-5321 alloy with damage tolerance^[10-26], involving the phase transformation, texture, microstructure evolution mechanism, strengthening and toughening mechanism, damage tolerance behavior and mechanical properties, etc, and great achievements have been obtained. In this work, the relationship between strength and toughness (impact toughness, fracture toughness) of Ti-5321 alloy was studied

Received date: June 25, 2022

Foundation item: National International Science and Technology Cooperation Project of China (2015DFA51430); National Natural Science Foundation of China (52101122, 51471136)

Corresponding author: Zhao Yongqing, Ph. D, Professor, Northwest Institute for Nonferrous Metal Research, Xi'an 710016, P. R. China, E-mail: trc@c-nin.com

Copyright © 2022, Northwest Institute for Nonferrous Metal Research. Published by Science Press. All rights reserved.

and reviewed in combination with the latest research results, in order to lay a foundation for the practical application of this alloy.

1 Relationship Between Strength and Impact Toughness of Ti-5321 Alloy

The Ti-5321 alloy used in this experiment was $\Phi 20$ mm hot rolled bar, which was forged from a 500 kg ingot and then hot rolled at 830 °C. The phase transition temperature of Ti-5321 alloy was 860 ± 5 °C. Two typical microstructures, bimodal microstructure (BM) and lamellar microstructure (LM), were obtained through the heat treatment processes shown in Fig.1. As shown in Fig.1a, in the heat treatment process of bimodal microstructure, the $\alpha + \beta$ phase region (830 °C) is selected for solid solution. The microstructure of BM can be seen in Fig.2a. Equiaxed α phase (α_{pe}) and rod-like α phase (α_{pr}) in the initial hot-rolled bar can be preserved during the solid solution process. And then, after the air-cooling process, metastable β phase can be obtained, in which fine secondary α phase (α_s) is precipitated and evenly distributed on the β matrix during aging. These uniformly distributed regions containing secondary α are usually called β transition structure (β_t). Fig.2b shows the microstructure of LM. After solid solution in the β phase region (900 °C), the furnace cooling rate of 0.01 °C/s is selected. The coarse lamellar α phase (α_{pl}) precipitates in the furnace cooling process which is arranged in parallel to form α colonies, and different α colonies can be staggered. After air cooling and subsequent aging, β transition structure (β_t) with uniform distribution of secondary α phase can be obtained.

Table 1 summarizes the parameters of α phase in two typical microstructures. It can be seen that the content of primary α phase α_p in BM is 10vol%, while that in LM increases to 60vol%.

Table 2 shows the tensile properties and V-notch impact toughness of the two typical microstructures at room temperature. The properties of Ti-5321 are closely related to the microstructure. BM shows high strength (tensile strength,

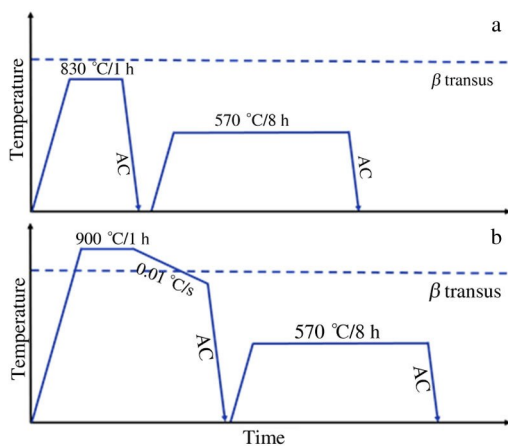


Fig.1 Heat treatment for two typical microstructures: (a) BM and (b) LM^[19]

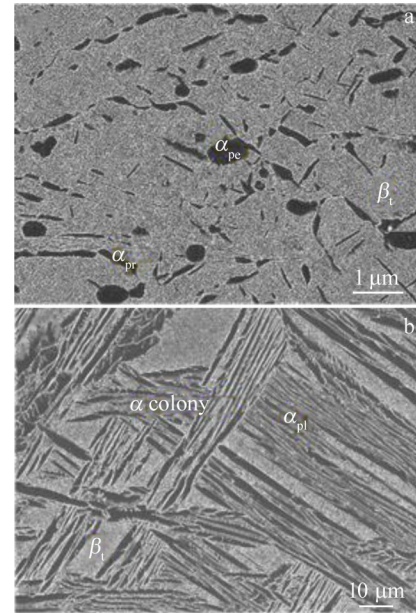


Fig.2 SEM images of two typical microstructures^[19]: (a) BM and (b) LM

Table 1 Microstructure parameters for BM and LM

Microstructure	Fraction of α_p /vol%	Diameter of α_{pe} /μm	Width of α_{pr} /μm	Width of α_{pl} /μm
BM	10	2.3 ± 0.6	0.88 ± 0.14	-
LM	60	-	-	1.9 ± 0.24

Table 2 Tensile properties and impact toughness of V-type notch at room temperature for two typical microstructures

Microstructure	UTS/MPa	EL/%	a_{kv} /J·cm ⁻²
BM	1296	12.3	12.9
LM	1052	14.5	37.5

UTS: 1296 MPa) and good plasticity (elongation, EL: 12.3%), but low impact toughness (a_{kv}). The strength of LM decreases with the increase in primary α phase content, but the plasticity and impact toughness increase, especially the impact toughness obviously increases. The relationship between strength and impact toughness is inverted.

Fig.3 shows TEM images of the two typical samples after tensile deformation. In BM, the main deformation characteristics of primary equiaxed α are deformation band and the dislocation pile-up at the interface (Fig.3a). Selective area electron diffraction analysis of the secondary α phase reveals the formation of nanoscale deformation twins inside secondary α phase (Fig.3b). When the local stress direction is parallel to the c -axis direction of the secondary α phase, the cylinder and basal slip cannot produce deformation along the c -axis, while the conical slip shows a high critical shear stress, and thus the twinning deformation in the secondary α phase provides the strain in c -axis direction. The twinning

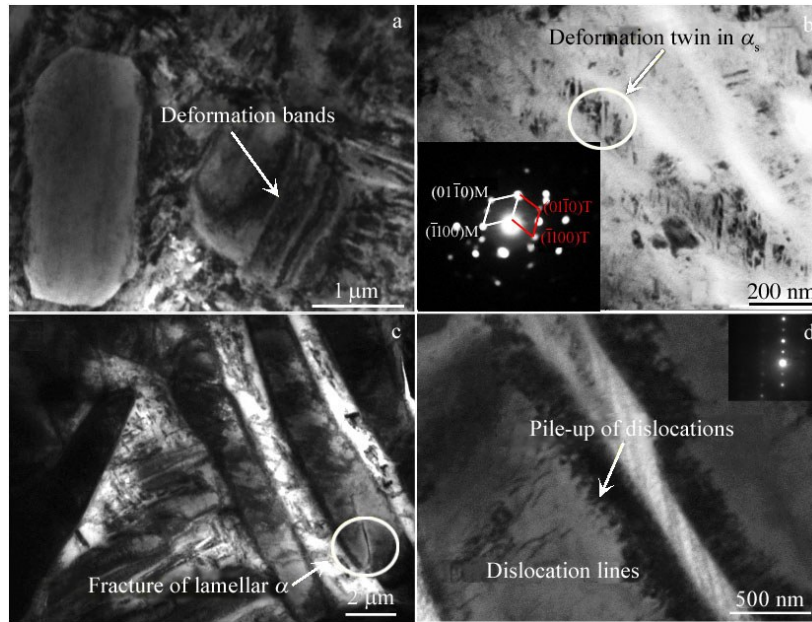


Fig.3 TEM images with SAED pattern shown in inset of Fig.3b of two typical microstructures after tension: (a, b) BM and (c, d) LM^[19]

deformation of secondary α phase can effectively improve the plasticity of this alloy. According to the relevant literatures of titanium alloys, twinning deformation is more likely to occur in the equiaxed α phase and lamellar α phase^[27,28], and the formation of nanotwins in secondary α phase is rarely reported so far. In LM, the lamellar α phase does not twist or deform, while only cracks can be found locally (Fig.3c). At the same time, parallel dislocation lines can be found inside the lamellar α and a large number of dislocations pile up at the interface (Fig.3d). In addition, high density dislocation can be found in the secondary α phase in both BM and LM, indicating that fine secondary α phase is an important microstructure characteristic to enhance the strength of this alloy.

The instrumented impact is used to test the impact property of two typical samples. The load-displacement curve obtained during instrumented impact is helpful for the deep analysis of their impact process. Fig. 4 shows the instrumented impact curves of two typical microstructures. The impact process can be divided into two stages by the maximum load F_m , namely, crack initiation stage and crack propagation stage. The load-displacement curve before F_m is integrated to obtain the crack initiation energy, while the load-displacement curve after F_m is integrated to obtain the crack propagation energy.

As can be seen from Fig.4a, the impact load-displacement curve of BM shows that in the crack initiation stage, the load increases with the increase of displacement. In the crack propagation stage, the load of BM drops sharply, so it can be seen that the crack growth energy is low. The impact load-displacement curve of LM curve is apparently different with BM, especially in the crack propagation stage. When the load reaches F_m , the load does not drop sharply, but shows a relatively slow process. The gradual decrease of impact load can significantly increase the impact displacement, and thus

increase the impact energy of LM. Finally, it can be concluded through the impact energy-displacement curve that the total impact energy increases with the change of the microstructure from BM to LM, and the impact toughness value also increases.

Fig. 5 shows the fracture morphology of the samples after impact test. By comparing the fracture morphology in Fig.5a and 5b, the fracture morphology of BM is relatively flatter compared with LM, indicating that the impact fracture mode has changed from brittle fracture of BM to ductile fracture of

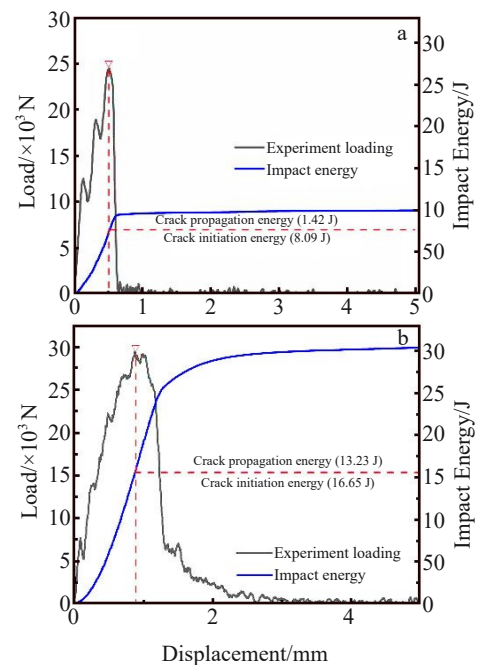


Fig.4 Load-displacement and impact energy-displacement curves of two typical microstructures: (a) BM and (b) LM^[19]

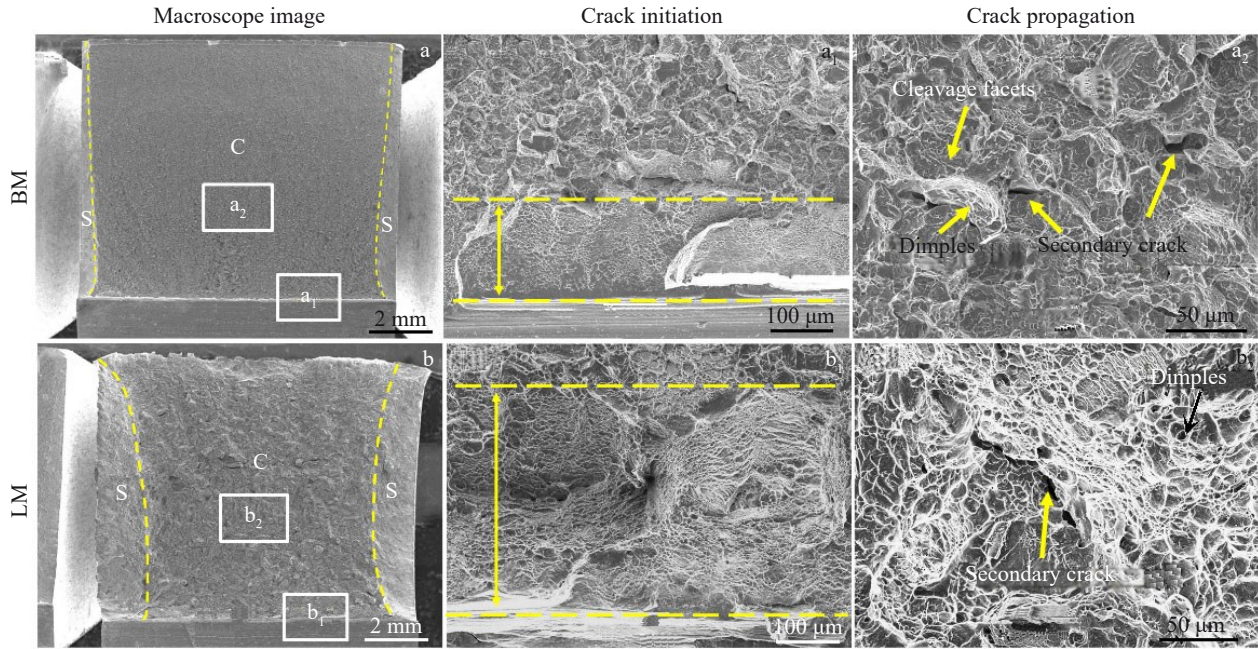


Fig.5 Impact fracture morphologies of two typical microstructures: (a, a₁, a₂) BM and (b, b₁, b₂) LM^[19]

LM. The fracture morphology of both the two microstructures can be divided into three typical regions, namely, crack initiation region, crack propagation region and shear region. Generally, the impact crack originates from the edge of the V-shaped notch and expands rapidly under the high strain rate of impact. Therefore, the small area close to the V-shaped notch is the crack initiation region, while the area far away from the V-shaped notch is the crack propagation region. As can be seen from Fig. 5a₁ and 5b₁, the initiation regions show the fracture morphology of cleavage plane and tearing edge. By comparing the size of the initiation region, it can be seen that the initiation region of BM is small, while the initiation region in LM is relatively large, indicating that the impact initiation energy is significantly improved for LM. The crack

propagation regions of Fig. 5a₂ and 5b₂ show the fracture morphology of dimples and secondary cracks. Comparing the impact propagation area of different microstructures, it can be seen that the impact propagation region of BM contains more cleavage planes in addition to dimples and secondary cracks (Fig.5a₂), while the dimples in LM are denser (Fig.5b₂), which is consistent with the fact that LM has a higher impact propagation energy in the impact curve.

Fig.6 shows the EBSD observations on the area beneath the fracture surface of LM. Crystallographic orientation and stress distribution can be obtained from the EBSD results. Different IPF colors represent different orientation relationships of phases. In Fig.6a, staggered α colonies in LM show different orientations, but the orientation of lamellar α phase within the

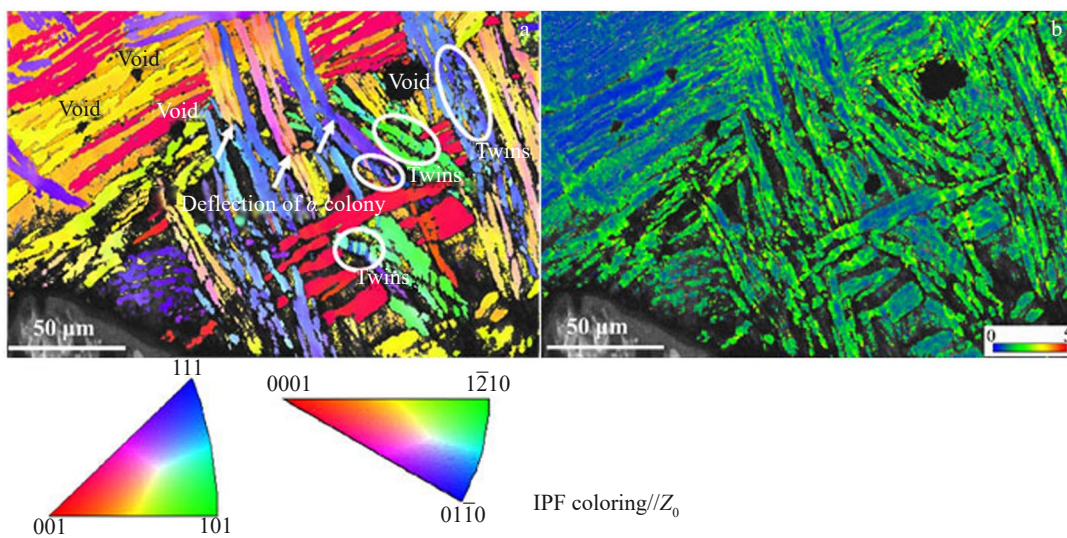


Fig.6 EBSD images of LM impact fracture profile: (a) IPF and (b) KAM^[19]

same α colony is consistent. The staggered α colonies grow in different directions, and have specific misorientation angles between adjacent α colonies due to the variant selection behavior, usually showing large angle grain boundaries between them. It is the misorientation and different growth direction between α colonies that can significantly change the crack growth path and then play an important role in preventing the crack growth. When the crack is significantly deflected, the local orientation of the α cluster near the crack is also deflected. As shown by the arrows in Fig. 6a, the IPF color of the twisted α lamellar is obviously changed. Fig. 6b is the KAM image of LM, which indicates the local stress distribution of the deformed samples. The blue areas represent the small degree of plastic deformation, and the green areas represent the large degree of plastic deformation. It can be found that higher KAM value exists near the crack, indicating that local plastic deformation dominates during the impact process. In addition to the interface of lamellar α , the KAM value inside α lamellar is also high, indicating that α colonies can bear large plastic deformation. Besides, high KAM value can also be found at the interleaving of α colonies and micro voids, showing that the interleaving distribution of α colonies can effectively hinder the crack propagation. Moreover, the IPF image of Fig. 6a shows the formation of deformation twins inside the α colonies.

Crack initiation energy and crack propagation energy are important performance indicators to characterize the resistance to impact load. The crack initiation energy is mainly consumed in the elastic and plastic deformation and crack formation of samples, while the crack propagation energy is mainly consumed in the plastic deformation and crack propagation at the crack front. Therefore, the crack initiation energy and propagation energy of Ti-5321 alloy are further analyzed in Fig. 7. Compared with BM, LM shows higher crack initiation energy, while BM shows significantly less crack propagation energy than LM (Fig. 7b). The relatively high crack initiation energy and propagation energy of LM make it possess the highest impact toughness. At the crack initiation stage, the primary α phase with larger size shows higher plastic deformation ability than the secondary α phase, so the increase in the primary α phase content (from BM ~10% to LM ~60%) significantly increases the crack

initiation energy. Once such an unstable impact crack is generated, the impact load will be significantly reduced, thus entering into the propagation stage, as shown in the load-displacement curve in Fig. 4. It can be seen that the initiation energy accounts for ~80% in BM and decreases to ~67% in LM. Therefore, the improvement of crack propagation energy is crucial to improve the total impact energy. In general, during the crack propagation process, the crack tends to bypass the equiaxed and lamellar α phases, which are relatively thick, and then deflects, presenting a tortuous crack propagation path. In this respect, the tailoring of LM aims to make a greater resistance to the propagation of crack, and to increase the tortuous degree of crack. The thick α colonies in LM represent a good effect on impeding and deflecting the dynamic impact crack due to its staggered distribution characteristic.

2 Relationship Between Strength and Fracture Toughness of Ti-5321 Alloy

The experimental Ti-5321 alloy is 120 mm billet, which is further forged in order to obtain the designed microstructure. In the modified forging stage, the conventional forging process is used to refine the grains. The finished forging stage is the decisive stage of microstructure construction. Near- β forging and β forging are used to obtain two typical microstructures (Fig. 8): bimodal microstructure (BM) and lamellar microstructure (LM). After forging, they are subjected to the same heat treatment process, which is $\alpha+\beta$ phase solution-aging heat treatment.

Table 3 shows the tensile properties (yield strength YS, ultimate tensile strength UTS, elongation EL, reduction of area RA and fracture toughness K_{IC}) of the two typical microstructures of Ti-5321 alloy after forging and heat treatment. The microstructure obviously affects the strength, plasticity and fracture toughness. In general, when the tensile strength is high, the fracture toughness is low. When the strength of BM reaches 1320 MPa, the elongation is 13.5%, and the K_{IC} exceeds 75 $\text{MPa}\cdot\text{m}^{1/2}$. When the K_{IC} of the LM exceeds 100 $\text{MPa}\cdot\text{m}^{1/2}$, the elongation is 11%, and its strength reaches 1216 MPa. In general, when the tensile strength is higher than 1250 MPa, the elongation is more than 10%, and

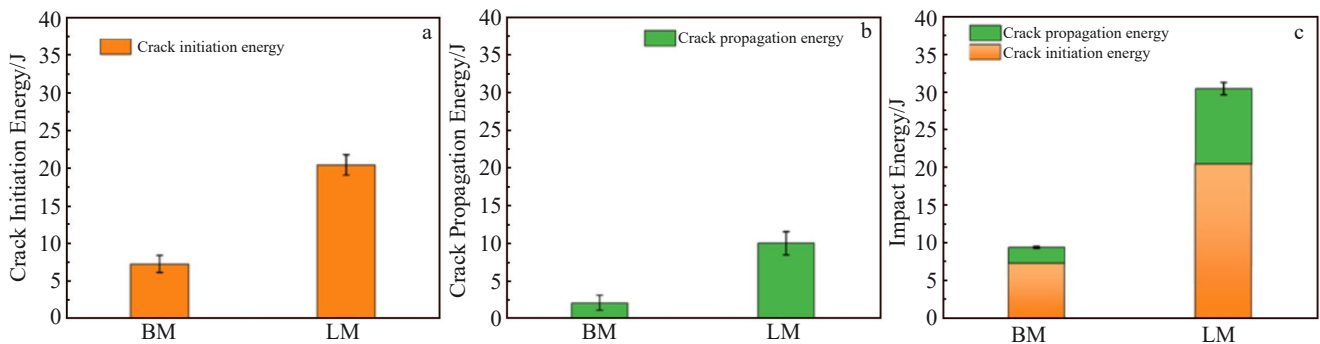


Fig. 7 Impact energy absorption at different stages of two typical microstructures: (a) crack initiation energy, (b) crack propagation energy, and (c) impact energy

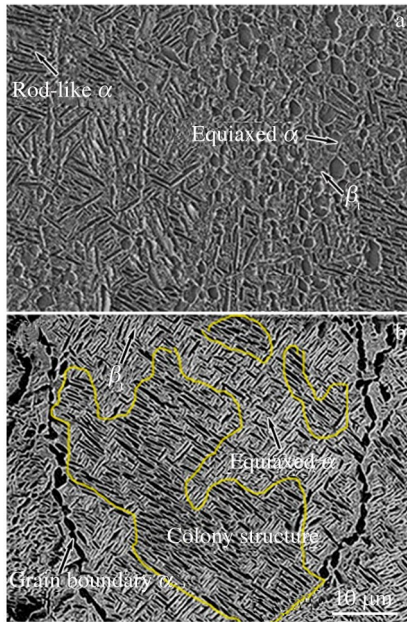


Fig.8 Two typical microstructures of Ti-5321 alloy after different forging followed by solution treatment and aging: (a) BM and (b) LM

the K_{IC} of the alloy is more than $76 \text{ MPa}\cdot\text{m}^{1/2}$, a good match of high strength, high plasticity and high toughness can be achieved.

It can be seen from Table 3 that the strength of the near- β forged BM is higher than that of the quasi- β forged LM, which is closely related to the cooling rate after forging. Water cooling after forging can inhibit the precipitation of secondary α phase at the cooling stage, and thus at the subsequent solution-aging treatment, finer lamellae α precipitates and induces stronger dispersion strengthening effect. Therefore, BM with water cooling heat treatment after forging shows higher strength. As for the quasi- β forged LM, its poor strength and plasticity are related to the high forging temperature. Because the forging temperature is 30°C higher than the phase transformation temperature, a large amount of grain boundary α phase precipitates along the β grain boundary during the forging process. When the plastic deformation takes place, slip is easy to occur at the interface of grain boundary α phase and β transition matrix, and the tendency of intergranular fracture increases^[29], which in turn reduces the strength and plasticity.

The roughness of the fracture surface of the two typical microstructures is $\text{LM} > \text{BM}$. Combined with the fracture toughness data in Table 3, it can be found that K_{IC} is positively

Table 3 Tensile properties and fracture toughness of Ti-5321 alloy of two typical microstructures

Microstructure	YS/ MPa	UTS/ MPa	EL/%	RA/%	K_{IC} / $\text{MPa}\cdot\text{m}^{1/2}$
BM	1280	1320	13.5	50	76.7
LM	1167	1216	11	40	102

correlated with the tortuous degree of crack propagation. The crack propagation path is shown in Fig. 9. Voids and microcracks are the main characteristics in the plastic region near the main crack. In BM, the microcracks mainly concentrate at the α_p/β_t interface (Fig. 9b). For LW, a large number of secondary cracks which are located between lamellar α can be found near the main crack (shown by arrows in Fig. 9c). During plastic deformation, the formation of these interlaminar secondary cracks and crack branches can consume a lot of energy and significantly improve the fracture toughness. Meanwhile, crack bridging can be found during crack propagation in lamellar α (seen in the white rectangle in Fig. 9c), while no crack is found in the bridging area (Fig. 9d). At the same time, there are almost no voids and microcracks in the plastic region near the crack in lamellar α . Instead, a large number of severely deformed lamellar α phases are distributed near the main crack (Fig. 9d). This may be closely related to the small degree of stress and strain concentration in LM and the strong deformation resistance of the α_p/β_t interface. In addition, the microscale inhomogeneity of LM makes the nucleation of voids more difficult, resulting in the formation of a large number of severely deformed lamellar α , which increases the energy consumption in the plastic region and improves the fracture toughness. Compared with BM, there are a large number of discontinuous β grain boundaries and α -colonies domains in LM. When the crack passes through the grain boundary or propagates along the lamellar α interface, the crack propagation direction will be deflected, resulting in the rougher crack propagation path than that in BM. As the roughness of crack propagation path increases, the energy consumed during crack propagation is relatively large, so the fracture toughness of LM is higher than that of BM.

Fig. 10a and Fig. 10b show the SEM images of the crack path and the corresponding IPF map of EBSD in LM. The crack mainly propagates alternately along and through the α colonies, and the staggered distribution of α colonies causes such a tortuous crack path. The crack path in Fig. 10b is further enlarged and redrawn in Fig. 10c. It can be seen that the crack passes through the $\alpha_{\text{col.(I)}}$ at first, and then deflects near the interface between $\alpha_{\text{col.(I)}}$ and $\alpha_{\text{col.(II)}}$. At the same time, the secondary crack forms and continues to grow along the previous direction. The misorientation between $\alpha_{\text{col.(I)}}$ and $\alpha_{\text{col.(II)}}$ is only 22° . The crack continues to propagate along $\alpha_{\text{col.(II)}}$ with a certain distance, then changes direction and starts to propagate perpendicular to the lamellar for a short distance, and finally re-propagates along the α lamellar until it encounters $\alpha_{\text{col.(III)}}$. Subsequently, crack propagates along $\alpha_{\text{col.(III)}}$, until it extends again to the interface of $\alpha_{\text{col.(III)}}$ and $\alpha_{\text{col.(II)}}$. Finally, the crack passes through the interface and begins to propagate along $\alpha_{\text{col.(II)}}$. Considering the slip behavior during plastic deformation, it can be found that most crack paths in the α colonies are parallel to the slip trace in the grain, which indicates that crack propagation is closely related to crystallographic orientation. In Fig. 10c, some cracks tend to propagate along the $(\bar{1}011) \langle \bar{1}2\bar{1}0 \rangle$, such as crack 1, 3, 5, 7. Some cracks tend to propagate along $(10\bar{1}0) \langle 1\bar{2}10 \rangle$, such as

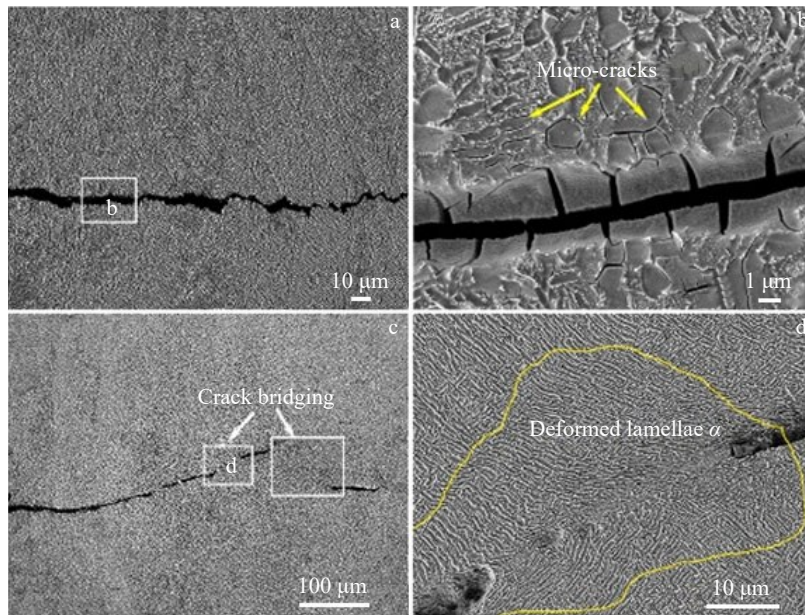


Fig.9 Crack path of two typical microstructures: (a, b) BM and (c, d) LM^[24]

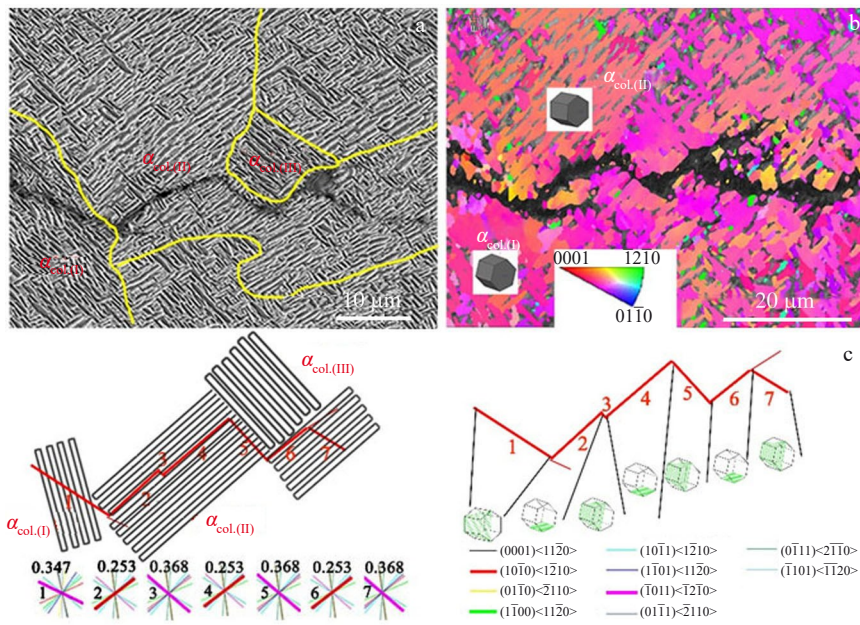


Fig.10 Crack path/colony microstructure interaction in LM^[24]: (a) SEM image of crack path; (b) IPF map of α phase; (c) schematic illustration of crack path/colony microstructure interaction

crack 2, 4, 6. According to the slip transfer criterion, slip is easy to be triggered on the slip surface with the largest Schmidt factor (μ) and the largest geometric coordination factor (m)^[30]. The Schmidt factor represents the ratio of shear stress to axial stress, while the geometric coordination factor reflects the misorientation between activated slip systems in adjacent grains. For the transgranular crack growth behavior, the propagation direction of crack 1 in $\alpha_{col(I)}$ and crack 3 in $\alpha_{col(II)}$ is parallel to $(\bar{1}011) \langle \bar{1}2\bar{1}0 \rangle$. The calculated Schmidt factors of $(\bar{1}011) \langle \bar{1}2\bar{1}0 \rangle$ in $\alpha_{col(I)}$ and $\alpha_{col(II)}$ are 0.347 and

0.368, respectively, which satisfies the slip transfer law of maximum Schmidt factor. For the intergranular propagation behavior, the Schmidt factor of $(10\bar{1}0) \langle \bar{1}2\bar{1}0 \rangle$ in crack 2, 4, 6 is only 0.253, which is not high. The calculated geometric coordination factor in $\alpha_{col(II)}$ between $(10\bar{1}0) \langle \bar{1}2\bar{1}0 \rangle$ and $(\bar{1}011) \langle \bar{1}2\bar{1}0 \rangle$ is 0.878, indicating that although the Schmidt factor of $(10\bar{1}0) \langle \bar{1}2\bar{1}0 \rangle$ is low, the arrangement between the two slip planes is well. Thus, the dislocation can easily pass from $(\bar{1}011) \langle \bar{1}2\bar{1}0 \rangle$ to $(100) \langle \bar{1}2\bar{1}0 \rangle$. Therefore, the slip behavior depends not only on the Schmidt factor, but also on

the geometric coordination factor between the adjacent slip planes.

Combined with Table 2 and Table 3, it can be seen that LM has a good match of strength, fracture toughness and impact toughness. Compared to BM, LM has the highest fracture toughness and impact toughness, as well as good plasticity. Although the BM has a good match between strength and fracture toughness, its impact toughness is low. There are intrinsic and extensional reasons for the high fracture toughness of LM. The intrinsic reason is affected by the deformation uniformity. LM has the lowest interfacial stress during plastic deformation, and the uniform strain distribution improves the crack propagation resistance. In terms of extensional reason, a large number of β grain boundaries and α clusters can cause the crack deflection and bifurcation in the maximum extent, which can reduce the effective stress intensity factor of crack tip and improve the toughness.

3 Conclusions

Some research results have been obtained on the strength, fracture toughness and impact toughness of 1200 MPa high strength and high toughness titanium alloy with damage tolerance. Microstructure obviously affects the strength and toughness of the alloy: the lamella microstructure (LM) has a good match of strength, plasticity, fracture toughness and impact toughness, while the bimodal microstructure (BM) also has a good match of strength, plasticity and fracture toughness, but its impact toughness is low. The changes of strength, fracture toughness and impact toughness are analyzed according to the microstructure evolution. According to the research progress of strength, fracture toughness and impact toughness of 1200 MPa high strength and high toughness titanium alloy with damage tolerance, the future development direction for high strength and high toughness titanium alloy with damage tolerance should be follows.

1) To develop higher strength and high toughness titanium alloys with damage tolerance, such as 1300 MPa titanium alloys with damage tolerance.

2) Further study on tailoring a stable microstructure with good match of strength, plasticity, fracture toughness and impact toughness.

3) Enhanced study on strengthening and toughening mechanism.

References

- 1 Kang Limei, Yang Chao. *Advanced Engineering Materials*[J], 2019, 21: 180 1359
- 2 James C Williams, Rodney R Boyer. *Metals*[J], 2020, 10: 705
- 3 Zhao Qinyang, Chen Yongnan, Xu Yiku et al. *Materials & Design*[J], 2021, 200: 109 457
- 4 Chen Wei, Liu Yunxi, Li Zhiqiang. *Journal of Aeronautical Materials*[J], 2020, 40: 63
- 5 Qu Henglei, Zhou Lian, Zhou Yigang et al. *Rare Metals Letter*[J], 2004, 23: 5
- 6 Boyer R R. *Journal of Metals*[J], 1992, 44: 23
- 7 Zhao Qinyang, Sun Qiaoyan, Xin Shewei et al. *Materials Science and Engineering A*[J], 2022, 845: 143 260
- 8 Huang Xu, Zhu Zishou, Wang Honghong. *Advanced Aeronautical Titanium Alloys and Application*[M]. Beijing: National Defense Industry Press, 2012 (in Chinese)
- 9 Zhao Yongqing, Ma Chaoli, Chang Hui et al. *Materials China*[J], 2016, 35(12): 914 (in Chinese)
- 10 Ren Lei, Xiao Wenlong, Chang Hu et al. *Materials Science and Engineering A*[J], 2018, 711: 553
- 11 Song Bo, Xiao Wenlong, Ma Chaoli et al. *Materials Characterization*[J], 2019, 148: 224
- 12 Song Bo, Chen Yu, Xiao Wenlong et al. *Materials Science and Engineering A*[J], 2020, 793: 139 886
- 13 Song Bo, Xiao Wenlong, Fu Yu et al. *Materials Letters*[J], 2020, 275: 128 147
- 14 Song Bo, Xiao Wenlong, Wang Junshuai et al. *Journal of Alloys and Compounds*[J], 2021, 879: 160 495
- 15 Gu B, Chekhonin P, Schaarschuch R et al. *Journal of Alloys and Compounds*[J], 2020, 825: 154 082
- 16 Gu Bin, Chekhonin P, Xin Shewei et al. *Materials Characterization*[J], 2021, 179: 111 297
- 17 Gu Bin, Chekhonin P, Xin Shewei et al. *Journal of Alloys and Compounds*[J], 2021, 876: 159 938
- 18 Wu Cong, Zhao Yongqing, Huang Shixing et al. *Journal of Alloys and Compounds*[J], 2020, 841: 155 728
- 19 Wu Cong, Zhao Yongqing, Huang Shixing et al. *Material Characterization*[J], 2021, 175: 111 103
- 20 Wu Cong, Zhao Yongqing, Sun Qiaoyan et al. *MATEC Web of Conferences*[J], 2020, 321: 12 005
- 21 Wu Cong, Zhao Qinyang, Zhao Yongqing et al. *Journal of Materials Science & Technology*[J], 2022, 103: 29
- 22 Wu Cong, Zhao Qinyang, Huang Shixing et al. *Journal of Materials Science & Technology*[J], 2022, 112: 36
- 23 Wang Huan, Zhao Qinyang, Xin Shewei et al. *International Journal of Fatigue*[J], 2021, 151: 106 348
- 24 Wang Huan, Zhao Qinyang, Xin Shewei et al. *Materials Science and Engineering A*[J], 2021, 821: 141 626
- 25 Wang Huan, Xin Shewei, Zhao Yongqing et al. *Materials Science and Engineering A*[J], 2020, 797: 140 080
- 26 Wang Huan, Zhao Yongqing, Zhao Qinyang et al. *Materials Characterization*[J], 2021, 174: 11 075
- 27 Qin Dongyang, Lu Yafeng, Guo Dizi et al. *Materials Science and Engineering A*[J], 2013, 587: 100
- 28 Huang Chaowen, Zhao Yongqing, Xin Shewei et al. *Journal of Alloys and Compounds*[J], 2017, 693: 582
- 29 Sauer C, Lütjering G. *Materials Science and Engineering A*[J], 2001, 319: 393
- 30 Luster J, Morris M A. *Metallurgical and Materials Transactions A*[J], 1995, 26(7): 1745

1200 MPa级高强高韧损伤容限钛合金强韧性研究进展

赵永庆¹, 吴 聪², 王 欢¹

(1. 西北有色金属研究院, 陕西 西安 710016)

(2. 陕西科技大学, 陕西 西安 710021)

摘 要: 高强高韧损伤容限钛合金是高强钛合金的重要研究方向, 本文重点研究、评述了1200 MPa级高强高韧损伤容限钛合金Ti-5321的拉伸强度与冲击韧性、断裂韧性的关系。Ti-5321合金的微观组织明显影响合金的强度和韧性。片层组织具有较好的强度、塑性、断裂韧性、冲击韧性匹配, 而双态组织也有较好的强度、塑性、断裂韧性匹配, 但冲击韧性低。结合微观组织演变分析了强度、断裂韧性、冲击韧性的变化规律, 并提出了高强高韧损伤容限钛合金的研究方向。

关键词: 钛合金; 高强损伤容限钛合金; 力学性能; 微观组织

作者简介: 赵永庆, 男, 1966年生, 博士, 教授, 西北有色金属研究院, 陕西 西安 710016, E-mail: trc@c-nin.com